Exp Fluids (2011) 50:597–611
DOI 10.1007/s00348-010-0950-9

RESEARCH ARTICLE

Laser-pulse interferometry applied to high-pressure fluid flow in micro channels

U. Iben · A. Morozov · E. Winklhofer · F. Wolf

Received: 29 January 2010 / Revised: 1 June 2010 / Accepted: 23 July 2010 / Published online: 24 August 2010
© Springer-Verlag 2010

Abstract The miniaturization of hydraulic systems together with ever increasing static and dynamic fluid pressure as is happening in fuel injection systems leads to complex flow effects with very high local and temporal pressure gradients. System optimization for hydraulic efficiency, components durability or spray formation quality needs the understanding of relevant flow properties. Fluid flow simulation models support such understanding, but with the complex nature of flow conditions, they are in need for precise and comprehensive verification and validation data. This work reports on measurement methods and analysis results for local fluid density and pressure measurements under overall stationary, highly turbulent and cavitating flow conditions in planar, optically accessed, model flow experiments. Laser-pulsed interferometry is applied for the measurement of fluid density fields under high spatial (~3 μm) and temporal (~5 ns) resolution. Interferometric imaging and image evaluation techniques provide ensemble mean pressure field data, local pressure fluctuation and differential pressure data. This yields information about local flow features such as flow vortex generation frequency, spatial size and shape of vortices and local pressure distribution inside of vortex structures. Features of bubble collapse process and corresponding pressure shock waves have been observed. The analysis method is applied to a forward-facing step and a target flow geometry. Experimental method, evaluation procedures and results are presented in this paper.

U. Iben (✉) · F. Wolf
Robert Bosch GmbH, Robert Bosch Platz 1,
70839 Gerlingen, Germany
e-mail: uwe.iben@de.bosch.com

F. Wolf
e-mail: Fabian.Wolf@de.bosch.com

A. Morozov · E. Winklhofer
AVL List GmbH, Hans-List-Platz 1, 8020 Graz, Austria
e-mail: Alexander.Morozov@avl.com

E. Winklhofer
e-mail: Ernst.Winklhofer@avl.com

1 Introduction

Modern diesel fuel injectors have small nozzle holes (diameter ~100 μm and length ~1 mm) in order to inject the fuel into the engine cylinder with high momentum. To fulfill the rigorous exhaust gas laws, very high injection pressure is used. The fluid flow under these conditions generates very complex structures. The flow fields are characterized by large local and time-dependent changes of flow properties such as density, pressure, temperature and velocity gradients, which can cause cavitation. Cavitation erosion on the component surfaces introduce restrictions for fuel delivery into the combustion chamber. The protection against cavitation erosion requires a detailed knowledge of the local flow fields including the mechanisms of cavitation generation and collapse of the cavitation clouds. Several publications with experimental results on turbulent flow structures and cavitation in water have been published, cf. Belahadji et al. (1995), Lui et al. (2008). A direct use of these results for diesel fuel is often not possible because of substantial differences of numerous fluid and hydraulic flow parameters, which lead to problems with the application of the similarity laws. Differences in pressure and velocity gradients, bubble sizes and vapor pressure, viscosity and density and typical geometrical sizes for water and diesel fuel flows have to be mentioned. Furthermore, simulation models need some

quantitative experimental database for verification and validation.

The following approach for experimental measurements is proposed:

1. The size of the flow geometry, the fluid type and hydraulic parameters are comparable to real fuel injector component sizes, cf. Iben and Morozov (2008).
2. Precise measurements of hydraulic boundary conditions with external pressure and temperature sensors, and mass flow measurements are included into the experimental procedure. A high-pressure throttle to fix planar geometries with an optical access has been developed for optical flow measurements under high-pressure conditions up to 1200 bar, cf. Winklhofer et al. (2001).
3. Optical methods for the determination of fluid density are the most appropriate because they are contactless, no tracers are needed and the flow field is not affected. The spatial and time-dependent density distribution plays an important role for the characterization of flow fields. Among optical methods, interferometry is the best and most accurate one for quantitative measurements of local density distributions, cf. Born and Wolf (1999), Ostrovsky et al. (1980).
4. The parameters of the optical measurements, i.e., necessary temporal and spatial resolution are determined by the flow parameters. Visualization of cavitating flow with transmission measurements is done to determine the corresponding optical conditions for further interferometric measurements. The interferometry is to be suited for fluid flow in small-sized geometries. A Nd:YAG laser, a CCD-camera and a modified Mach-Zehnder interferometer are used for interferogram recording. Turbulent flow structures with a size of 20 μm and bubbles with a diameter of 5–10 μm can be visualized for flow regimes with maximal flow velocities of approximately 100m/s.
5. The quantitative study of shear layer and flow turbulence properties for single-phase liquid flow as well as weak cavitating flow is possible by interferometry. The approach allows to study the relations between the flow geometry, the hydraulic boundary conditions, the local density fluctuations and the cavitation formation.

The methods of holographic and digital interferometry are described in Goodman (1968), Hipp et al. (2004), Ostrovsky et al. (1980), Vest (1979), Woisetschlaeger et al. (1998). The digital holographic methods allow to compare phase distributions, which exist at different definite times, cf. Collier et al. (1971), Ostrovsky et al. (1980). Therefore, it is possible to increase the accuracy of phase measurements and to reduce the quality of applied optical elements significantly. In this paper, the methods have been improved and adapted for special conditions of turbulent partially cavitating micro-flows that need extremely high spatial and temporal resolution for quantitative measurements of local flow parameters. The improvements include the hardware as well as the measurement and evaluation procedures. The quantitative relations between measured phase values and local flow pressure and temperature are derived for diesel fuel.

2 Theoretical considerations

The principles of wave front phase distribution measurements and relations between measured phase values and local fluid density are described later. The possibilities of local pressure and temperature determination from fluid density values are discussed.

2.1 Phase distribution measurements

The phase change of a laser beam with a wave length λ due to wave propagation along the z-axis inside a medium with the length l and the refraction index $n_i(x, y, z)$ is defined by

$$\Phi_i(x,y) = \frac{2\pi}{\lambda}\int_0^l n_i(x,y,z)\mathrm{d}z, \tag{1}$$

neglecting diffraction effects, cf. Born and Wolf (1999), Ostrovsky et al. (1980). The index i is the image counter, which is connected with a particular object state at temporal moment t_i for the object beam. The coordinates (x, y) are the position in the recorded image.

Following Born and Wolf (1999), Ostrovsky et al. (1980), the relative phase change of a laser beam can be measured with interferometry respectively to the so-called reference beam. The recorded intensity distribution $I_i(x, y)$ for the area of overlapping and coherent reference and object beams is determined by

$$I_i(x,y) = I_{i0}(x,y) + K_i(x,y)\cos\left[\Phi_{i,\mathrm{Ref}}(x,y) - \Phi_{i,\mathrm{Obj}}(x,y)\right] \tag{2}$$

with the mean intensity $I_{i0}(x,y)$ and the contrast factor $K_i(x, y)$. $\Phi_{i,\mathrm{Ref}}(x, y)$ is the phase of the reference wave on the image plane and $\Phi_{i,\mathrm{Obj}}(x, y)$ is the phase of the object wave at the same plane. The relative phase difference between the reference and the object beams at the registration plane is denoted by $\delta\Phi_i(x, y)$:

$$\delta\Phi_i(x,y) = \Phi_{i,\mathrm{Ref}}(x,y) - \Phi_{i,\mathrm{Obj}}(x,y). \tag{3}$$

If some definite angle β is introduced between optical axis of the reference and the object beams, then the

regular high carrier frequency of interference fringes $\nu_{\text{carrier}} = (\sin\beta)/\lambda$ appears with the intensity distribution described by eq. (2) additionally to relatively low frequency of intensity modulation due to spatial variations of object properties.

It has been shown in Goodman (1968), Woisetschlaeger et al. (1998), Hipp et al. (2004) that the phase difference $\delta\Phi_i(x, y)$ can be calculated using the two-dimensional fast Fourier transformation for intensity distribution $I_i(x, y)$ of eq. (2), which can be written, using the Euler, identity as:

$$I_i(x,y) = I_{i0}(x,y) + G_i(x,y) + G_i^*(x,y) \quad \text{with} \tag{4}$$

$$\begin{aligned} G_i(x,y) &= \frac{1}{2}K_i(x,y)e^{i\cdot\delta\Phi_i(x,y)} \quad \text{and} \\ G_i^*(x,y) &= \frac{1}{2}K_i(x,y)e^{-i\cdot\delta\Phi_i(x,y)} \end{aligned} . \tag{5}$$

The term $G_i(x, y)$ on the right hand side of eq. (4) contains information on the phase distribution $\delta\Phi_i(x, y)$. Following Goodman (1968), the resulting signal for the spatial frequency domain can be described by the following relation:

$$i_i(\nu_x,\nu_y) = i_{i0}(\nu_x,\nu_y) + g_i(\nu_x,\nu_y) + g_i^*(\nu_x,\nu_y). \tag{6}$$

In eq. (6), each item is the Fourier transform of the corresponding terms in eq. (4). The terms $g_i(x, y)$ and $g_i^*(x, y)$ in eq. (6) are connected with the phase difference, whereas the focus is on the term $g_i(x, y)$. A mask around $g_i(x, y)$ is determined for the spatial frequency domain in a next step. All values outside the mask are set to be zero. Then, the inverse Fourier transform is applied to the spatial frequency signal domain with the described mask, cf. eq. (6). According to that, the term for $G_i(x, y)$ in eq. (5) is determined. The phase distribution is calculated by the inverse Fourier transform from the filtered signal $G_i(x, y)$ according to:

$$\delta\Phi_{i-\text{step}}(x,y) = \arctan\left(\frac{Im(G_i(x,y))}{Re(G_i(x,y))}\right). \tag{7}$$

The obtained step-wise or modulo 2π phase distribution must be subjected to some smoothing procedure to obtain the final continuous phase distribution $\delta\Phi_i(x, y)$ described by eq. (3), cf. Hipp et al. (2002).

The measurement procedure requires experimental recording of two image sequences. The first one corresponds to the undisturbed state (reference state) of the object without flow (no external pressure applied). The second one corresponds to the flow conditions for definite external pressure. The reference beam and complete measurement geometry remain the same for both sequences. Direct subtraction of these two phase distributions, cf. eq. (3), leads to the phase distribution, which is completely determined by object changes between recordings. The first sequence without flow has a constant refractive index on the complete visible object area. For the second measurement with flow, each local phase value depends on local refractive index. Due to linearity of all applied transformations and eqs. (1–7), the following equation for this final phase distribution is obtained:

$$\begin{aligned} \delta\varphi_{\text{flow}}(x,y) &= \delta\Phi_{\text{flow}}(x,y) - \delta\Phi_0(x,y) \\ &= \frac{2\pi}{\lambda}\int_0^l [n_{\text{flow}}(x,y,z) - n_0]\mathrm{d}z. \end{aligned} \tag{8}$$

For a resting fluid under predefined conditions, the object refractive index and the phase distribution are denoted by n_0 and $\delta\Phi_0(x,y)$ respectively. The local value of refractive index is n_{flow} and phase is $\delta\Phi_{\text{flow}}(x, y)$ for flowing fluid. The presented procedure eliminates all the wave front distortions due to optical elements. It is only sensitive to flow changes between two flow states, if the recording system remains without any changes during the complete measurement procedure.

2.2 Relations between phase delay and medium parameters

The relation between the local medium density ρ and the refractive index n is as follows

$$\rho = \frac{W}{A}\frac{n^2-1}{n^2+2}, \tag{9}$$

where A is the molar refractivity and W is the molecular weight, cf. Born and Wolf (1999). A linearization of eq. (9) at the reference point (ρ_0, n_0) leads to

$$\rho(x,y,z) = \rho_0\left(1 + \frac{6n_0}{(n_0^2-1)(n_0^2+2)}[n(x,y,z) - n_0]\right). \tag{10}$$

From eqs. (8) and (10), a relation between averaged density along the z-axis and the interferometrically measured phase variation can be derived:

$$\frac{\partial\bar{\rho}(x,y)}{\partial\varphi(x,y)}\cdot l = \rho_0\frac{3\lambda n_0}{\pi(n_0^2-1)(n_0^2+2)}, \tag{11}$$

where λ is the laser wavelength and l the depth of the object. The depth-averaged density is denoted by $\bar{\rho}$. Using eq. (11) and the experimentally determined values for diesel fuel density $\rho_0 = 834\,\frac{\text{kg}}{\text{m}^3}$ on the reference point $p_0 = 1$ bar and $T_0 = 288$ K, the refractive index $n_0 = 1.46$ and the wave length $\lambda = 532$ nm, the partial derivative of the depth-averaged density by the phase change is as follows

$$\frac{\partial\bar{\rho}}{\partial\varphi}\cdot l = 0.132\frac{\text{kg}\cdot\text{mm}}{\text{m}^3\cdot\text{radian}} \quad \text{for} \quad p_0 = 1\,\text{bar} \quad \text{and} \quad T_0 = 288\,\text{K}. \tag{12}$$

Eq. (12) is used for the calculations of relative density distributions in the flow field using measured phase data. The

absolute density values for calibration can be calculated at some reference flow positions with independently measured pressure and temperature. The liquid density depends on the static pressure p and the temperature T, which can be described by a first-order approximation of the thermodynamic equation of state:

$$\rho(p,T) \approx \rho(p_0,T_0) + \left.\frac{\partial\rho}{\partial p}\right|_{(p_0,T_0)}(p-p_0) + \left.\frac{\partial\rho}{\partial T}\right|_{(p_0,T_0)}(T-T_0). \tag{13}$$

The coefficients in eq. (13) have been determined for BP-15 diesel fuel using the bulk modulus value for diesel from Boehman et al. (2003) and the thermal expansion coefficient from Budwig (1994). They are equivalent to the following values:

$$\left.\frac{\partial\rho}{\partial p}\right|_{T=293\,\mathrm{K}} = 0.058\frac{\mathrm{kg}}{\mathrm{m}^3\cdot\mathrm{bar}} \quad \text{and} \quad \left.\frac{\partial\rho}{\partial T}\right|_{p=50\,\mathrm{bar}} = -0.59\frac{\mathrm{kg}}{\mathrm{m}^3\cdot\mathrm{K}}. \tag{14}$$

Combining eq. (12) and eq. (14), the following formulas are obtained, which determine the relations between the measured phase values and the independent local flow parameters such as the pressure p and the temperature T:

$$\frac{\partial p}{\partial\varphi}\cdot l = 2.28\frac{\mathrm{bar}\cdot\mathrm{mm}}{\mathrm{radian}} \quad \text{and} \quad \frac{\partial T}{\partial\varphi}\cdot l = -0.224\frac{\mathrm{K}\cdot\mathrm{mm}}{\mathrm{radian}}. \tag{15}$$

For a thickness $l = 0.3$ mm of the model geometry and a laser wave length $\lambda = 532$ nm, the partial derivatives are $\frac{\partial p}{\partial\varphi} = 7.6\frac{\mathrm{bar}}{\mathrm{radian}}$ and $\frac{\partial T}{\partial\varphi} = -0.75\frac{\mathrm{K}}{\mathrm{radian}}$. The typical accuracy of digital interferometry in fringe shifts is $\delta X = \lambda/20$, i.e., $\delta\Phi = 2\pi/20 \approx 0.3$ radian. Therefore, it is possible to measure a pressure difference of $\delta p > 2.5$ bar and a temperature difference of $\delta T > 0.25$ K for the described operation conditions. Phase variations are directly measured experimentally. The local density variations in the liquid flow can be calculated using eq. (12). In general, some additional information or independent measurements are necessary for the separation of pressure and temperature influences on density variation. For well-defined flow regimes such as inflow domains of a throttle or jet flow areas, separated considerations of the pressure or the temperature in eqs. (13) and (15) are possible.

3 Experimental setup

3.1 Hydraulic part of setup

The hydraulic system is designed to supply well-defined in- and outflow conditions on the high-pressure throttle. The system supports variable and precisely controlled macroscopic boundary flow conditions, i.e., inlet pressure and temperature, and the outlet pressure. The measurements of all mentioned flow parameters in addition to the outlet temperature and the time-averaged mass flow rate are realized.

The experimental facility includes a pressure supply system, the high-pressure throttle, a back flow circuit and measurement sensors and devices, cf. Winklhofer et al. (2001). The installed hydraulic system guarantees a variable inlet pressure with pressure fluctuations smaller than 1 bar. The flow geometry is included in a plane steel plate with a thickness of 300 μm. It is sandwiched between two sapphire windows. One window includes a hydraulic inflow and a hydraulic outflow. The pressure as well as the temperature is measured at these positions. Fig. 1a displays the high-pressure throttle. The sketches of the studied hydraulic geometries are presented in Fig. 1b and c.

3.2 Optical system and components

The optical system consists of the following main parts: light sources, a modified Mach-Zehnder interferometer with an imaging objective and a recording CCD-camera. The optical arrangement is schematically presented in Fig. 2. A flash lamp (Nano Twin Flash / High-Speed Photo System triggered by nanolite driver) with $\delta t_{\mathrm{lamp}} = 15$ ns is used for flow visualization measurements.

A Nd:YAG laser (New Wave Solo III 15 Hz) with a wavelength $\lambda = 532$ nm, a pulse duration $\delta t_{\mathrm{las}} = 5$ ns and a pulse energy $E_{\max} \sim 50$ mJ is used for interferometry. The laser operates at the TEM00-mode, which supplies a high spatial coherence of the beam and several centimeters of temporal coherence length. The last-mentioned circumstances ensure the simplicity of the interferometer adjustments and high contrast of the interference fringes.

A telescopic system (T) with a spatial filter with diameter $D = 30$ μm is used to remove coherent noise from the wave front and to ensure a uniform Gaussian intensity profile with a diameter $\sim$10mm at the object plane. The beam splitter (BS) divides the beam into the reference and the object beam. The object beam passes the high-pressure throttle and the objective. Due to the angle between the reference and the object beam, a carrier fringe distribution with a spatial frequency ν_{carrier} is created on the CCD-camera window, cf. Born and Wolf (1999), Goodman (1968). The modified Mach-Zender interferometer (MZI) has some differences from a classical one. The mirror M4 replaces the normally used second beam splitter that ensures simple adjustment and optimal determination of interference fringes carrier frequency and orientation without a distortion of the object beam. The angle between the reference and the object beam is not limited by BS

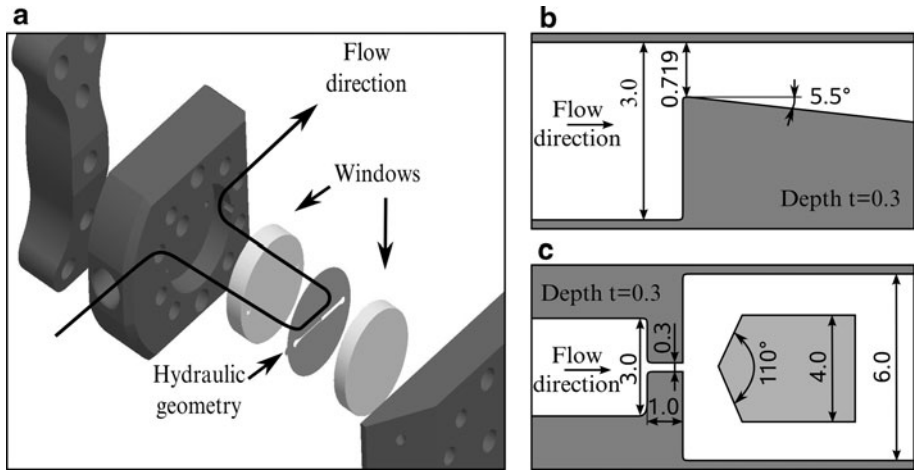

Fig. 1 **a** Experimental setup of the high-pressure throttle with optical access and hydraulic inlet and outlet, **b** forward-facing step flow geometry, **c** target geometry, all geometrical sizes are in mm

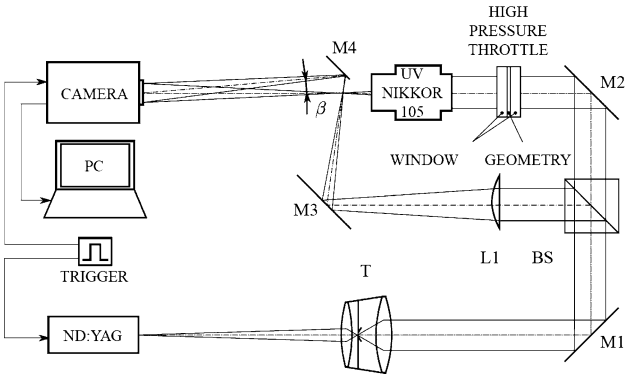

Fig. 2 Experimental setup with optical components and data acquisition tools

aperture. Therefore, high fringe frequencies and arbitrary orientations are available. Additionally, the intensity on the CCD-camera is twice as high in comparison with the classical MZI. The mirror M4 is installed near to the focal points of lens L1 and Nikkor-objective in such a way that the reference beam focus reaches the edge of the mirror M4, which in turn does not influence the object beam.

The objective (achromatic UV Nikkor 105 mm) produces a magnified and sharp projection of the flow geometry on CCD-camera window. The objective has a broadband antireflection coating and variable focal length. It can be used for both transmission measurements with white light and interferometry with laser light of $\lambda = 532$ nm. Magnifications up to $M = 7$ are possible that supply the corresponding scaling factors during recording in the range 0.8–6.0 μm/pixel. According to Born and Wolf (1999), the spatial resolution can be as good as $d_{\mathrm{res}} = 0.6\ \lambda/\mathrm{NA} = 3$ μm, where NA $\approx$ 0.1 is the numerical aperture of the objective. Low noise cooled 12-bit, 1280 × 1024 pixel CCD-cameras, PCO SensiCam and LaVision FlowMaster3 are used in the measurements. The low noise cooled CCD-camera has a minimal temporal gate of $\delta t_{\mathrm{cam}} > 400$ ns, which is too large. The light pulse duration determines the real recording time, i.e., the temporal resolution in this case. All the applied lenses and beam splitters have an antireflection coating for 532 nm. The sapphire windows do not have a coating. The optical paths for the reference and the object beams are equalized with several millimeters accuracy to achieve high fringe contrast.

3.3 Triggering and flow measurements

Either a Nd:YAG laser or a flash lamp is used for the measurements. The CCD-camera, light sources and the hydraulic measurement sensors are triggered by a multichannel pulse generator. The camera gate duration is set to 1 μs. The laser pulse is adjusted to occur in the middle of the camera opening time interval to avoid all possible jitter effects and own camera and laser internal pulse delays. CamWare V2.03—software from PCO Imaging is used for the recording procedures. A frequency of four frames per second is used for undisturbed recording of the complete 1280 × 1024 pixel images. The hydraulic data measurements (pressures, temperature, mass flow) are started together with the first camera pulse of the measurement series. At a sample rate of 50 KHz, 1000 samples are recorded for the pressure transducers. The sample rates for mass flow and temperature transducers are lower. The high-frequency turbulence fluctuations are not resolved with these hydraulic measurements, so that time-averaged values are presented during the recording time.

4 Measurement procedures and evaluations

4.1 Measurement procedure

The spatial and temporal resolutions for experimental measurements must be defined with respect to the flow

parameters. Parameters of fluctuations and cavitating structures are not known a priory. The required spatial resolution results from transmission measurements and is defined by the size of small visible turbulent and cavitating structures of $d < 10$ μm. Table 1 displays the relations between expected flow processes and temporal resolutions necessary for their study. Exposure time of $t_{exp} < 10$ ns is required to study the process of vortex generation and shock waves in detail.

Transmission and interferometry measurements are carried out with 100 images in series for each hydraulic condition and each particular optical magnification. Both types of measurements require a recording of reference series without flow. One reference series before serial measurements with flow and one reference series after flow measurements are recorded to control possible mechanical shifts during experiments. An optical magnification of $M = 1.2$ is used to get some general overview of the complete flow region. The maximal possible magnification of $M = 7.3$ with a corresponding spatial resolution of 3 μm is used to obtain detailed information, e.g., the properties of the narrow shear layers and the small-sized vortex structures. The corresponding boundary hydraulic conditions (p_{in}, p_{out}, T_{in}, T_{out}) and integral mass flow $\dot{m}$ are recorded with external sensors at all times.

During interferometrical measurements, an angle $\beta = 1°$ between the reference and the object beam is used to supply the carrier frequency of interference fringes. If this angle is large enough, i.e., the maximal spatial eigen object frequency $\nu_{max} < \frac{1}{3} \cdot \nu_{carrier}$, cf. Collier et al. (1971), then all three items in eq. (6) are spatially separated in the frequency domain. The maximal fringe frequency is limited by the pixel size of the CCD-camera because the minimal number of independent points needed for fringe recording should not be less than 5 pixels/fringe. At the same time, "effective" object spatial frequencies, which correspond to the image plane (CCD-camera window), are diminished inverse proportionally to the magnification with respect to the original object plane. Both the angle β and the object magnification M are specified in such a way that the mask around $g_i(x, y)$ in eq. (6) produces proper separation of the selected term and does not restrict the original spatial resolution, which is determined by the objective quality. All the described evaluation options are realized with the software package 2d-inf[1], which includes single and statistical image processing and fast two-dimensional Fourier transform.

Table 1 Local displacements during exposure time for different flow events

Light source			Nd:YAG	Flash lamp	He–Ne
t_{exp} (ns)		1	5	15	400
Process	Velocity (m/s)	Spatial shift (μm)			
Flow motion	100	0.1	0.5	1.5	40
Shock waves	1,200	1.2	6	18	480

4.2 Statistical image evaluation

Evaluation procedure supposes single-shot image evaluations and statistical serial evaluations. The measurement data are a two-dimensional matrix with a dimension of 1280 × 1024 points. A sequence of images is recorded. The images are denoted by the index i. The following statistical procedures have been realized for both transmission and interferometry measurements, which corresponds to single-shot intensity or phase distributions $\psi_i(x, y)$. Due to the linear properties of the evaluation procedures and the thermodynamic equation of state, the statistical parameters for mean and standard deviation for density, pressure and temperature values can be derived consequently by the corresponding mean $\psi_{mean}(x, y)$ and standard deviation phase values $\psi_{RMS}(x, y)$. A total number of images per series of $N = 100$ is chosen in order to get meaningful statements of derived statistical values such as standard deviation. Transmission measurements are mainly qualitative and do not need higher accuracy. The accuracy of quantitative interferometric measurements (2.5 bar) is worse than the obtained RMS-values (1.2 bar), which are $\sim 1/\sqrt{N = 100}$.

The differential single-shot density distributions

$$\psi_{i-\mathrm{diff}}(x, y) = \psi_i(x, y) - \psi_{\mathrm{mean}}(x, y) \tag{16}$$

allow to analyze among other things the vortex generation frequency for vortices perpendicularly orientated to the flow direction. The statistical evaluation procedures are applied to the forward-facing step flow and the target flow.

4.3 Evaluation procedure

4.3.1 Transmission images

The following procedure is used to reduce the influence of illumination spatial non-uniformity and light source temporal instability on transmission image quality. First of all, the mean serial intensity distribution is calculated for the reference object state without flow. The number of recorded images in a series is $N = 100$. Then, for flow conditions, each single-shot transmission image is subjected to a point-to-point normalization procedure using this mean reference intensity distributions. The normalized single-shot intensity is called transmission I_t and varies at a range of $0 < I_t < 1$. The reference intensity remains constant for

[1] The software has been developed at AVL List GmbH Graz, Austria.

small areas with an accuracy of ±1.5%, which is mainly influenced by the noise of the CCD-camera. The normalized single-shot intensity displays a higher fluctuation level of ±4%. The procedure reduces the local signal fluctuation by a factor of ~3. The curve for the cavitation density dependence on light transmission values is not calibrated. The method gives qualitatively good results for flow visualization. Small gas bubbles reduce transmission to $I_t \sim 0.2-0.3$. Cavitation is always visible as very dark (black) areas in the liquid flow with $I_t = 0$. Turbulent structures, shear layers and shock waves are also visible mainly due to the optical vignetting of the refracted light. The transmission values are much higher, i.e., $I_t \sim 0.8-0.9$. These flow features are visible as gray. Statistical evaluations show information about the location and shapes of cavitation zones, shear layers and shock waves.

4.3.2 Interferometry

The evaluation procedure for single-shot interferograms follows the steps illustrated in Fig. 3. The interferogram (or intensity distribution, Fig. 3a) contains a high-frequency structure of interference fringes due to the angle $\beta = 1°$ between reference and object laser beams. The nearly straight lines of fringes are slightly distorted by flow inhomogeneities. Then the interferogram is subjected to a two-dimensional fast Fourier transform (FFT) according to eqs. (4)–(6). A result is presented in Fig. 3b. The right-top edge corresponds to the term $g_i(v_x, v_y)$ in eq. (6). A mask (filter) around this item is set in the spatial frequency domain, cf. Fig. 3c. It maintains valid data inside the marked contour and sets all the values outside to zero. The mask can have an arbitrary shape. For example, small regions inside the large external mask contour can be deactivated (see Fig. 3c). The large signal at these regions is connected with an unfavorable intensity modulation due to a secondary light reflection on the camera window. The mask covers all the first-order spatial frequency object area, which is visible in the frequency domain and determined by the objective aperture as described in Sect. 4.1. The mask does not restrict the original spatial resolution of the recorded image.

The spatial frequency spectrum (Fig. 3b) with the applied mask (Fig. 3c) is subjected to a Fourier inversion. The step-wise or modulo-2π phase distribution according to eq. (7) is obtained in Fig. 3d. This discontinuous distribution is subjected to the smoothing procedure with a Branch-cut option, cf. Hipp et al. (2002). The result of the smoothing continuous phase distribution describes the phase difference between the reference and the object beams for the present flow conditions, cf. Fig. 3e. The corresponding reference state (without flow) phase distribution must be subtracted according to eq. (8), and a resulting flow phase distribution is received, cf. Fig. 3f. The last distribution presented in Fig. 3f is free of distortions due to imperfection of optical elements and only depends on the object difference.

The complete list of evaluation operations to obtain the final pressure and temperature distributions from recorded interferograms includes the following evaluation steps:

1. Calculation of the single-shot reference state phase distributions for all serial images with N=100 and further calculations of the mean reference state phase distribution and RMS. Reference RMS-phase distribution is used for the control of evaluation quality of all serial single-shot evaluations.
2. Calculation of the single-shot flow phase distributions following subtraction of mean reference state phase from each single-shot flow distribution and subsequent calculation of the mean flow phase and RMS-phase distributions.

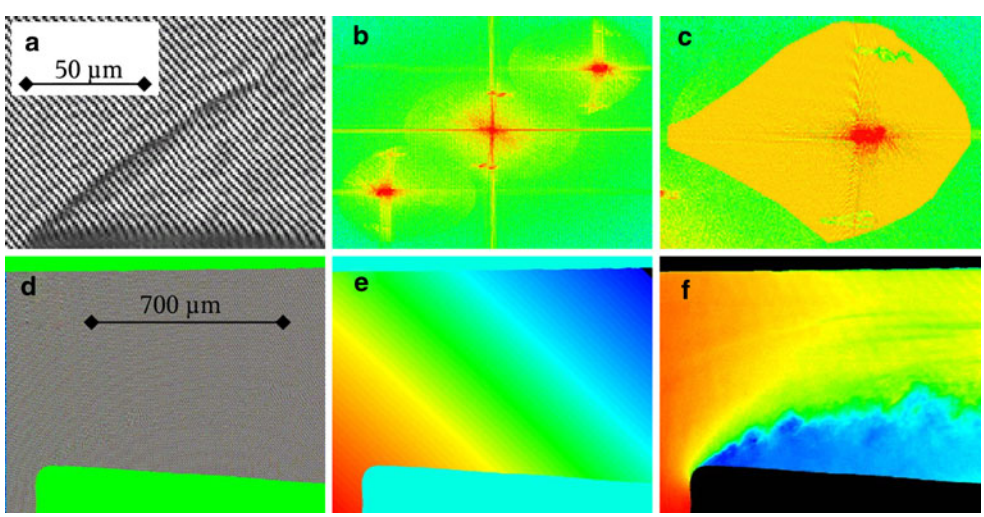

Fig. 3 Interferogram evaluation process: **a** original flow interferogram, magnified part near to inlet edge, **b** spatial frequency spectrum, **c** mask at the frequency domain, **d** modulo 2π phase distribution, **e** continuous phase distribution, **f** final phase distribution after reference phase subtraction

3. Calculation of the differential flow phase distributions for single-shot flow distributions with subtraction of mean flow phase distribution, according to eq. (16).
4. Measurements of maximal (positive and negative) phase fluctuation amplitudes at each single-shot flow distribution and subsequent statistical evaluations of measured maximal phase fluctuations with calculations of mean maximal fluctuation, RMS, minimal and maximal serial value.
5. Calculation of the depth-averaged local density, pressure and temperature values according to Sect. 4.2.

4.3.3 The Abel transform

Generally, one can only obtain depth-averaged values along the beam path with interferometry. In some special cases, when the object has cylindrical or spherical symmetry, it is possible to apply the procedure of Abel transform and to reconstruct the real radial spatial phase distribution, cf. Hipp and Reiterer (2003). The inverse Abel transformation determines the relation between the measured depth-averaged phase distribution $F(y)$ on the recording plane (CCD-camera chip) along the y-axis passed through the center of the object symmetry and the real radial phase distribution, which is denoted by $f(r)$. Assuming that $f(r)$ drops to zero more quickly than $1/r$, the inverse Abel transform is given by

$$f(r) = -\frac{1}{\pi}\int_r^{\infty} \frac{\mathrm{d}F(y)}{\mathrm{d}y}\frac{\mathrm{d}y}{\sqrt{r^2 - y^2}}. \tag{17}$$

The corresponding software package is available free on the web site of TU Graz and is used in the presented evaluations, cf. Hipp and Reiterer (2003). The Abel transform is used for a detailed analysis of spherically symmetrical shock waves, which are generated due to the collapse of cavitating bubbles.

4.3.4 Accuracy of the phase, density, pressure and temperature measurements

The local phase variations in flow areas with constant pressure p and temperature T (inlet reference area) for single-shot distributions are measured with an accuracy of $\delta\varphi = \pm 0.3$ radian or $\sim \lambda/20$. The measured phase accuracy is even better for differential images, i.e., $\delta\varphi = \pm 0.2$ radian or $\sim \lambda/30$. The density is calculated accurately using eq. (12). The values p_0 and λ are known precisely, n_0 depends on fluid type and on λ. The accuracy of n_0 is $\sim 1\%$. Pressure and temperature are derived from density values by eq. (14). In the case that one variable (pressure or temperature) is exactly known, the accuracy of the other one can be obtained directly from phase accuracy and eq. (15). The corresponding values for the presented experimental conditions are $\delta p = 2.3$ bar and $\delta T = 0.23$ K considering single-shot images. The absolute accuracy of pressure and temperature calculations depend on accuracy of the used values for liquid compressibility and thermal expansion, which are taken from Boehman et al. (2003), Budwig (1994). They depend on the liquid type and the local pressure and temperature. Additional verification of these values is made using the measured total phase difference between inlet and outlet flow parts and external sensors data. The literature and measured data are in a very good agreement with an accuracy of 3%. As already mentioned, the total derivative of density is a function of two independent variables p and T. Therefore, the accuracy is determined by the individual accuracy of pressure and temperature. The pressure and temperature external sensors must be located as close as possible to the area of the optical access. These data are used for the calibration of the conditions on the flow boundary domains. Hereby, the initial values p_0 and T_0 on the flow inlet and the flow outlet of the geometry are determined. The corresponding inaccuracy of the hydraulic measurements can be estimated to $\delta p < 1$ bar and $\delta T < 0.5$ K.

5 Results and discussions

Results of the presented optical measurement techniques are discussed on a forward-facing step and a target flow. The focus is on the analysis of the local flow fields, the pressure distribution around cavitating flow structures and the estimation of the amplitudes of shock waves generated by collapsing cavitation clouds. The transmission light measurements for cavitation visualization are done with a white light flash lamp and an exposure time of $t_{\mathrm{exp}} = 15$ ns.

5.1 Forward-facing step flow

The forward-facing step flow is utilized to analyze the shear layer flow without and with weak cavitation. The flow in front of the step is laminar. The step leads to a non-uniform acceleration of the fluid flow. Consequently, a shear layer is generated. It contains a flow instability[2]. Behind it, vortices and turbulent structures are generated, transported downstream with the flow field and decay. The pressure inside the vortices decreases and can lead to cavitation against the difference between the inlet and outlet pressure.

[2] Kelvin-Helmholtz-instability, which is independent of the fluid viscosity.

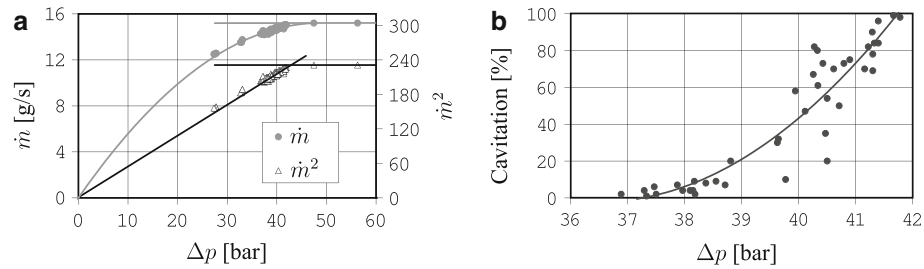

Fig. 4 **a** Hydraulic data—integral mass flow $\dot{m}$ and $\dot{m}^2$ as a function of pressure difference Δp; **b** cavitation statistics against Δp

5.1.1 Boundary hydraulic conditions and cavitation onset

The inlet pressure and the inlet temperature are fixed by $p_{\text{in}} = 100$ bar and $T_{\text{in}} = 308$ K. The outlet pressure p_{out} is variable. The integral mass flow rate $\dot{m}$ as a function of the pressure difference $\Delta p = p_{\text{in}} - p_{\text{out}}$ is measured, cf. Fig. 4a. The behavior of the integral mass flow rate contains two typical parts. The left part at low-pressure difference Δp represents the single phase liquid flow, which is described by the Bernoulli equation[3]. The right horizontal part represents the cavitating flow, when the integral mass flow rate is blocked by low density cavitating steam bubbles. It is denoted by the so-called choked flow, cf. Koivula (2000). The transition point (called Cavitation Critical Point—CCP) between two parts is sharp, and it is shown by the curve of $\dot{m}^2(\Delta p)$.

5.1.2 Cavitation visualization with light transmission measurements

The light transmission measurements are performed to determine the properties of cavitation onset depending on pressure boundary conditions. The results show the spatial location, the shape and the size of cavitating structures.

In each case, $N = 100$ images have been recorded for a fixed pressure difference Δp and a fixed inlet temperature T_{in}. The number of images with cavitating structures with respect to the overall number of images in series, i.e., cavitation probability, is presented in Fig. 4b. The cavitation probability grows nonlinear with respect to the pressure difference $\Delta p = 7$–42 bar, cf. Fig. 4b. There are no images with cavitation for a pressure difference of $\Delta p < 36$ bar. In contrast to it, 100% of the images display cavitation at $\Delta p > 42$ bar. The pressure difference of $\Delta p = 42$ bar corresponds to the CCP-point on the integral mass flow curve shown in Fig. 4a.

An example of the recorded images with cavitation is presented in Fig. 5a. Cavitation clouds occur in 40% of the series images. The cavitation structures are represented as dark areas in the single-shot transmission images. The images are recorded with a magnification of $M = 7.3$, a spatial resolution of $R \sim 3$ µm and a scaling factor of SF = 0.92 µm/pixel. Cavitation is generated at the end of the narrow shear layer behind the inlet edge and spread out with the flow downstream. Cavitation structures have different complex sizes and shapes. Three main types of structures are observed. These are small bubbles with a diameter of $d \sim 5$–10 µm, long narrow vortex structures with a length of $l \sim 50$–150 µm and a diameter of $d \sim 5$–10 µm and large "clouds" with a size of $d \sim 100$–200 µm. The shear layer directly on the step and following vortex structures are also visible due to optical vignetting of refracted light. The result of statistical mean transmission is presented in Fig. 5b. The standard deviation distribution where the blue color is always liquid or steam and the red color stands for high probability of liquid/gas transition is presented in Fig. 5c. The beginning of cavitation corresponds to the highest density fluctuation area behind the shear layer generated on the step.

5.1.3 Measurement procedure validation with continuous wave laser interferometry

The preliminary measurements have been done with a continuous wave He–Ne laser to test the complete measurement and evaluation procedure for interferometry and to check quantitative relations, i.e., eq. (15), derived in Sect. 2.2, which determines the relation between optically measured phase difference and local flow pressure and temperature. The exposure time $t_{\text{exp}} = 400$ ns is determined by the minimal digital camera gate duration, cf. Iben and Morozov (2008). Measurements are done with a low optical magnification $M = 1.16$ in order to obtain the complete flow field, when the optically visible area comes close to the positions of external pressure and temperature sensors. The complete measured phase difference is quantitatively compared with the calculated phase values using eq. (15) for the pressure difference ($\Delta p = 38$ bar) and temperature difference ($\delta T = 1.9$ K), which were measured with corresponding external sensors. The contribution of pressure to the complete phase difference is twice as large as the temperature contribution. Measured RMS-density fluctuations display a maximum 1.8 mm behind the step. It is reasonable to suppose that the pressure changes happen mainly direct close behind the step edge at

[3] Bernoulli equation: $p + \frac{\rho}{2}v^2 = \text{const}$, internal energy is assumed to be constant.

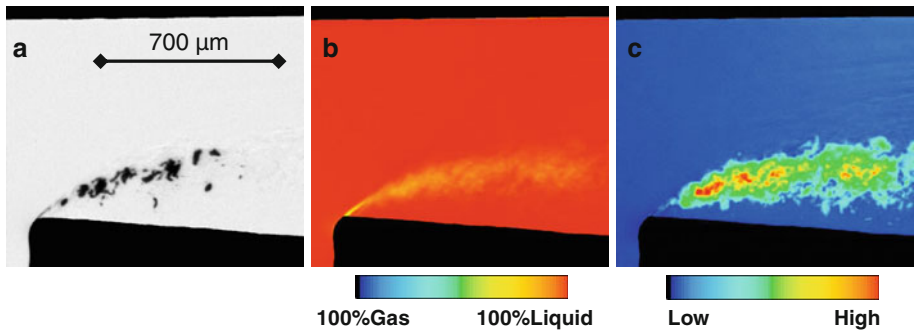

Fig. 5 **a** Single-shot cavitation distribution, **b** mean cavitation density, **c** cavitation standard deviation. $p_{in} = 100$ bar, $p_{out} = 60$ bar, $T_{in} = 308$ K

$L \leq 2$ mm and the temperature changes due to turbulence dissipation and flow thermalization occur downstream. These measurements and estimations are necessary for further study at high magnification without direct contact to the reference area.

5.1.4 Density and pressure distributions measurements with pulsed laser

To obtain detailed data of turbulence generation, interferograms are recorded with a Nd:YAG laser. The parameters are the following: a pulse length of $t_{exp} = 5$ ns, a high magnification of $M = 7.3$, a scaling factor of $SF = 0.92$ µm/pixel and a spatial resolution of ~ 3 µm. Hydraulic conditions are chosen near to the CCP, i.e., $p_{in} = 100$ bar, $p_{out} = 60$–63 bar, $T_{in} = 308$ K. Cavitation structures are contained in a small amount of images of these measurements series.

The single-shot pressure distribution is presented in Fig. 6a, where the shear layer and the flow instability is in evidence. The mean pressure distribution is presented in Fig. 6b. The local mean pressure in the recirculation area is much lower than the outlet pressure p_{out} but higher than the vapor pressure p_v of the fluid. The differential pressure distribution is calculated according to eq. (16) and is shown in Fig. 6c. It is visible that the pressure fluctuations are generated in the shear layer and are growing in size downstream the flow. The pressure standard deviation distribution is presented in Fig. 6d. Pressure fluctuations display a local maximum along the line of the shear layer. The large-scale features of fluctuations are comparable to former results obtained with a larger exposure time of $t_{exp} = 400$ ns. Finer turbulent structures can be observed with a short exposure time, e.g., shear layer structures with a diameter of 15–25 µm behind the step.

Additionally, the maximal positive and negative fluctuation amplitudes for each serial single-shot differential pressure distribution are analyzed. These values are measured for each single-shot image independently on location at this image. The measured maximal amplitude values are, in turn, subjected to statistical evaluation. Corresponding results for mean, RMS, minimal and maximal values of pressure fluctuations for single-shot distributions are presented in Table 2 for different hydraulic conditions. This fluctuation statistics is additional and different from RMS-statistics, cf. Fig. 6d, which represents the fluctuations at definite locations of the flow field.

Temporal averaging is negligible for short exposures of $t_{exp} = 5$ ns, cf. Table 1. The obtained data are the real instant local depth-averaged pressure values. Positive and negative fluctuations have the same magnitude and grow slightly together with pressure difference. Pressure standard deviations display a very stable magnitude of $\sim 20\%$ of the mean value for all measurement series. The maximal measured pressure amplitudes in the presented series are approximately twice as high as the mean fluctuation amplitudes, cf. Table 2.

Using an exposure time of $t_{exp} = 5$ ns, the shear layer is visible as a nearly straight line, see Fig. 7. It is stable in place and is not subject to spatial fluctuations. The definite thickness of the standard deviation distribution at the area of the inlet shear layer (± 3 µm) is partially due to small mechanical vibrations of the experimental setup during the measurement procedures. The measured length of the shear layer is $L_{sl} \approx 70$ µm. The development of turbulence structures are observed at the end of this stable line, cf. Fig. 7a. The diameter of the first vortex directly behind the step can be estimated by a length of 15–25 µm, cf. Fig. 7c. The pressure amplitude of this vortex is estimated to be $p_{turb} = \pm 25$ bar using serial differential pressure distributions. There are depth-averaged values with respect to the geometry depth of $l = 300$ µm. Therefore, local pressure fluctuations could be even higher.

5.1.5 Estimation of turbulence generation frequency on the step

The differential pressure distributions display quasi-periodical vortex structures generated behind the step, cf. Fig. 8a. The pressure fluctuations grow in size downstream of the flow. Fig. 8b shows the pressure fluctuations along the white line sketched in the differential single-shot

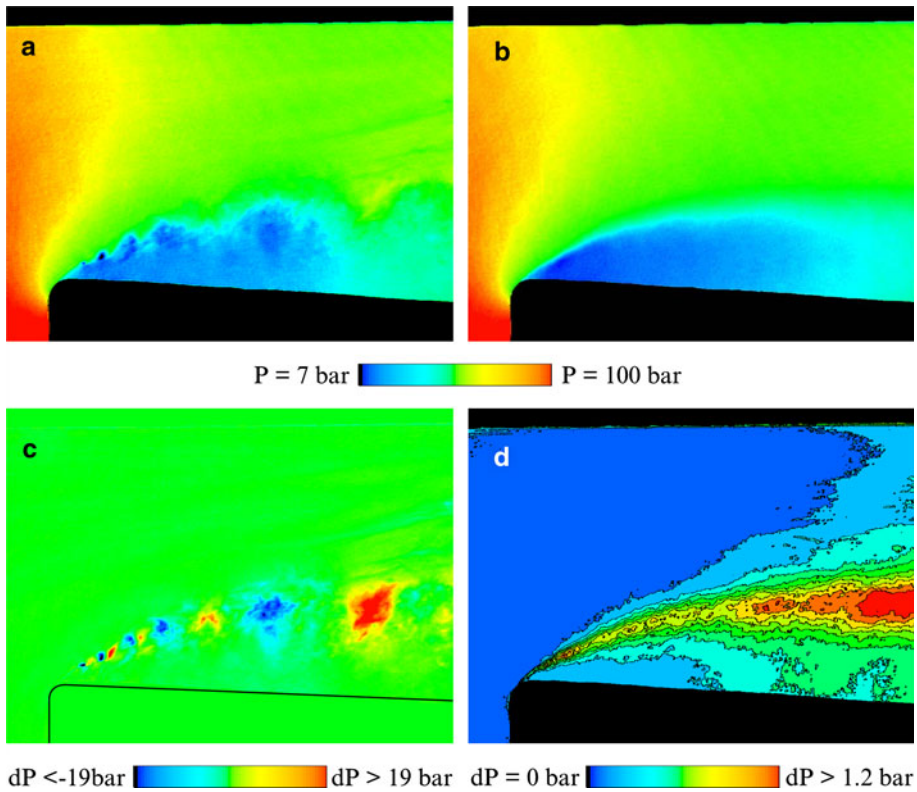

Fig. 6 Pressure distributions with high optical magnification $M = 7.3$: **a** Single-shot pressure distribution for image counter $n = 37$, **b** mean pressure distribution p_{mean} for $N = 100$, **c** differential pressure distribution p_{diff} for image counter $n = 37$, **d** pressure standard deviation p_{RMS}. $p_{in} = 100$ bar, $p_{out} = 63$ bar, $T_{in} = 298$ K

Table 2 Statistical parameters of the measured pressure fluctuations

Fluctuation amplitudes (bar)	100/59		100/60		100/61		100/63	
	−Δp	+Δp	−Δp	+Δp	−Δp	+Δp	−Δp	+Δp
Mean	24	26	25	24	25	23	23	22
Standard deviation	5	6	6	5	5	5	5	5
Min.	39	12	44	13	38	13	48	15
Max.	13	46	15	36	16	38	14	38

pressure distribution given in Fig. 8a. The line has the same position as the serial maximal standard deviation of the pressure.

The spatial period between the first two pressure minimums of the vortices behind the step is $\delta S = 55$ µm. The temporal period can be estimated by $T = \delta S / v_{Bern} = 55$ µm/94m/s $= 0.59$ µs. Thereby, v_{Bern} is the averaged velocity on the step estimated by the Bernoulli equation. The separation frequency of the vortices is $f = T^{-1} = 1.7$MHz.

5.1.6 Pressure fluctuations and cavitation onset

The minimal local mean value of depth-averaged pressure values p_{Recirc} in the recirculation area is determined against the pressure difference Δp and presented in Fig. 9a. In this procedure, only images without cavitation are considered. These mean values are always larger than the vapor pressure p_v for $\Delta p \leq 42$ bar $= \Delta p_{CCP}$. On the other hand, cavitation clouds occur in the shear layer. The single-shot pressure distribution is presented in Fig. 9c. The corresponding mean value of pressure is given in Fig. 9d. The pressure distribution on the evaluation line is plotted in Fig. 9b. It shows that the pressure mean value is always larger than the minimal occurring single-shot pressure values, which can reach the vapor pressure p_v[4]. These pressure values are the cores of vortices generated behind the step and flowing downstream. The evaluations show that the mean value of pressure of the complete flow field as well as on the evaluation line does not provide information of the cavitation generation. Cavitation is a phenomena on very small time and spatial scales especially near the CCP. The high transient behavior of the cavitation generation is given in Fig. 4b as well as in the chart of Fig. 9b.

5.2 Target hydraulic geometry

The interaction of turbulence generation, cavitation onset and shock waves is studied on the target geometry. The collapse of cavitating flow structures such as single bubbles or steam-filled vortices leads to shock waves propagating in the fluid. These shock waves play an essential role in the cavitation erosion process, cf. Franc (2009), Brennen (1995). The presented example shows the different sequences of the

[4] It is assumed that the fluid cannot adjust tensile strength.

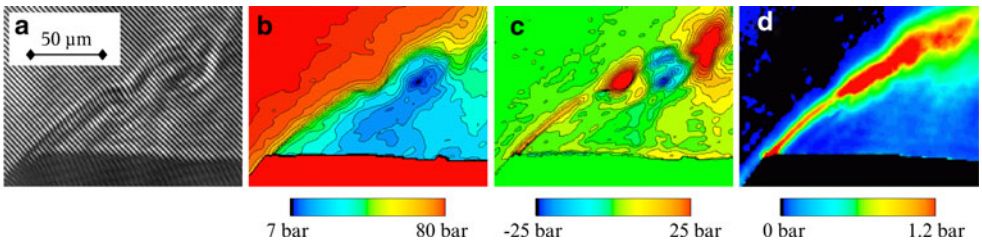

Fig. 7 Shear layer and first instability for high magnification and exposure time $t_{exp} = 5$ ns: **a** original image, **b** density distribution, **c** differential single-shot density ρ_{diff}, **d** RMS of density. $p_{in} = 100$ bar, $p_{out} = 59$ bar, $T_{in} = 316$ K, counter $n = 1$

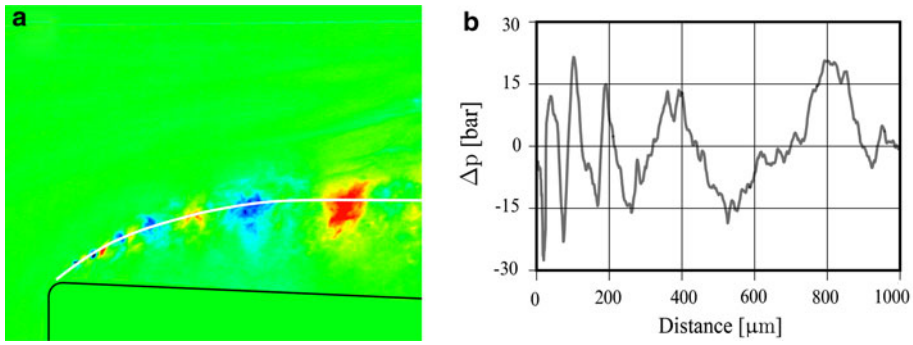

Fig. 8 **a** Fluctuation generation frequency—estimation from differential pressure distribution at the beginning of the step and downstream, **b** pressure distribution on the white line. $p_{in} = 100$ bar, $p_{out} = 63$ bar, $T_{in} = 308$ K, image number $n = 57$

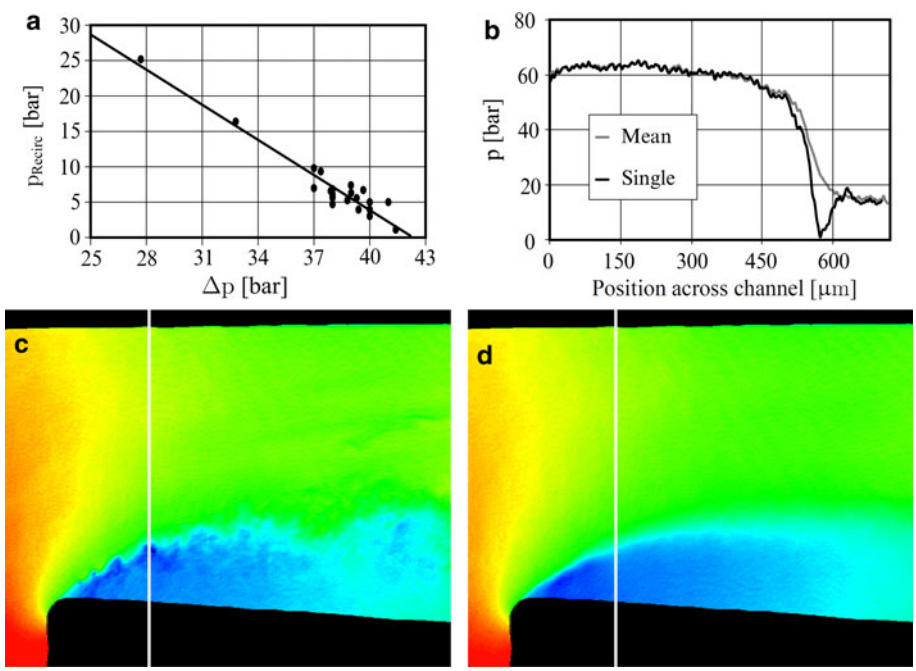

Fig. 9 **a** Mean pressure values in the recirculation area as a function of pressure difference Δp, **b** pressure distribution measured on the evaluation line—mean and single-shot pressure, **c** single-shot pressure distribution—image counter $n = 59$, **d** depth-averaged mean pressure distribution. **c**, **d** $p_{in} = 100$ bar, $p_{out} = 61$ bar

cavitation process beginning with the cavitation generation in the throttle, the following shear layer and finished by cavitation disappearances flow downstream due to bubble cloud collapse.

5.2.1 Flow visualization with transmitted light technique

The hydraulic conditions are chosen in a way so that cavitation in front of the target occurs in 100% of the recorded images. Cavitation occupies the boundary layers near to the walls of the throttle and is divided into two parts behind the throttle outlet and fills out the space near to the target surfaces, cf. Fig. 10a. The top of the target remains cavitation free.

The traces of spherical waves are detected in 20% of the serial images in the whole area between throttle and target. Figure 10 shows some of the typically observed shock waves generated by collapsing cavitation clouds and

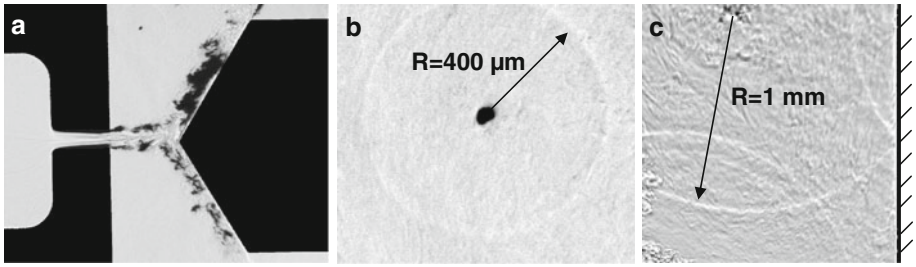

Fig. 10 Shock wave visualization with transmission measurements. **a** shingle-shot image of cavitating flow with bubble collapse event, **b** detail—spherical shock wave with cavitating gas bubble in the center; **c** large radius waves with reflection from the wall. $p_{in} = 336$ bar, $p_{out} = 36$ bar, $T_{in} = 303$ K

bubbles and their intensive interaction. The shock waves are generated in flow areas with high RMS-values of cavitation distribution. The nearly spherical shock waves display different diameters. In several cases, a steam bubble is clearly visible in the middle of the spherical wave front, cf. Fig. 10b.

5.2.2 *Density distribution measurements with interferometry*

Density distributions are measured with interferometry for the target flow. The hydraulic conditions are $p_{in} = 400$ bar, $p_{out} = 100$ bar and $T_{in} = 303$ K to prevent cavitation in a first step. The main results are presented in Fig. 11. The mean density distribution for a low optical magnification of $M = 1.6$ is presented in Fig. 11a. It covers the complete flow area of interest. Here, both variables – pressure and temperature – play a role for the density variations. Density changes are mainly due to a pressure drop in the channel (flow acceleration), momentum loss in the shear layers, and an increase in pressure in front of the target top (due to flow deceleration by the target surface). The temperature is mainly responsible for density changes on the broad area behind the throttle, where flow thermalization occurs. The RMS-density distribution is presented in Fig. 11b, which is obtained with intermediate optical magnification $M = 2.8$. The highest density RMS-values are obtained at the free flow region behind the throttle. The mean density

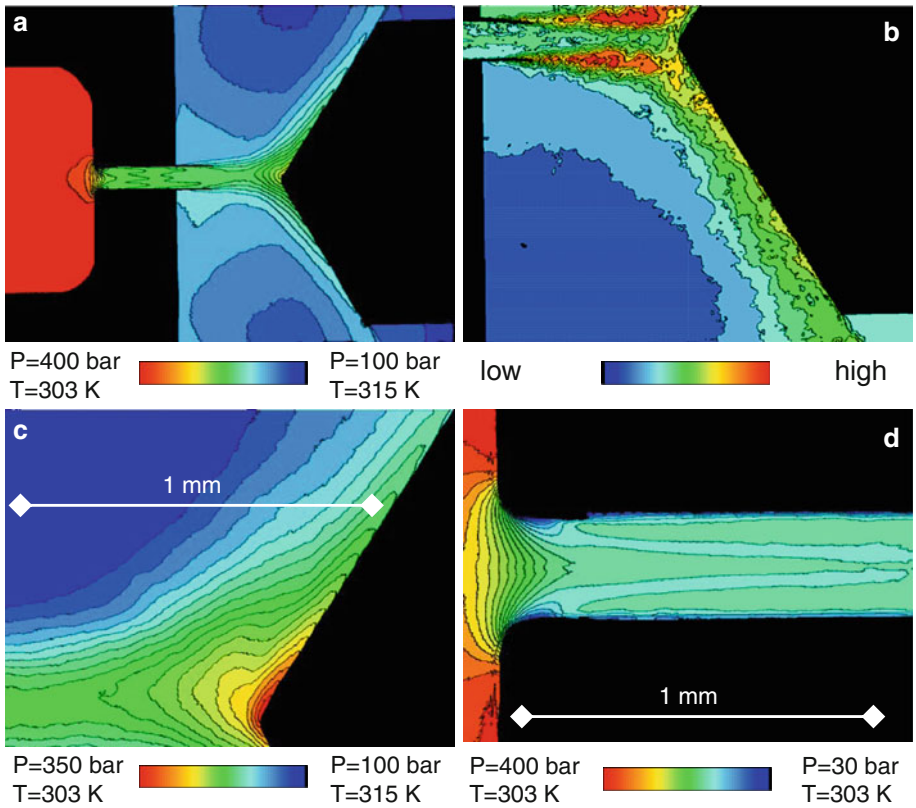

Fig. 11 Target geometry: **a** mean density distribution with low optical magnification $M = 1.6$, **b** RMS-density distribution with $M = 2.8$, **c** mean density distribution near to the target top with $M = 7.3$, **d** mean density distribution in the channel area with $M = 7.3$, $p_{in} = 400$ bar, $p_{out} = 100$ bar, $T_{in} = 303$ K

distribution near to the target top is presented in Fig. 11c, which is obtained at a high magnification $M = 7.3$ and a spatial resolution of 3 μm. The secondary static pressure maximum is nicely visible near the target top. This maximum is due to the flow deceleration on the target top. The pressure drop along the target surface is due to the following flow acceleration.

The single-shot differential pressure distribution near to the target top is calculated for the high optical magnification $M = 7.3$. The temperature influence on the density function is neglected in the present evaluations. The statistical parameters of the measured pressure fluctuations on the target behind the throttle are presented in Table 3. The mean amplitudes of the fluctuations are $\delta p = \pm 70$ bar. The maximal measured value of single-shot negative fluctuation is $\delta_{\mathrm{pmax}} = -122$ bar and exceeds the outlet pressure p_{out}. This value is physically not possible. This extreme high value is a result of the neglecting of the temperature increase in the turbulent layers, which is not taken into account in density–pressure calculations.

The throttle has a rounded inlet geometry that strongly reduces turbulent structures inside the throttle, cf. Fig. 11d. After the pressure drop on the inlet part, the pressure has a very uniform distribution in the complete throttle cross-section. Only two small linear local maxima are visible along the complete length. The lower density values in the boundary layers near to the throttle walls are due to the liquid warming in this regions based on the turbulent viscous interactions of the flow with the throttle walls. This effect is also shown by the RMS pressure distribution, where the maximal density fluctuations occur near to the throttle walls. The estimated thickness of the boundary layers is about 20–30 μm.

Table 3 Local pressure fluctuations at the target area

Fluctuation amplitudes	−Δp (bar)	+Δp (bar)
Mean	69	70
Standard deviation	14	13
Minimum	122	43
Maximum	38	106

The boundary conditions of the flow field are changed to achieve cavitating flow in a next step, cf. Fig. 12. The measurements with a higher optical magnification of $M = 2.8$ and $SF = 2.4$ μm/pixel are then performed. In this case, the throttle outlet and half of the target are optically accessible, cf. Fig. 12a. Furthermore, valid differential density data for the areas without cavitation have been obtained. An example of the fringe distortion by a cavitating bubble is presented in Fig. 12b. The evaluated differential phase distribution is shown in Fig. 12c. This distribution is a depth-averaged one. Supposing the spherical symmetry of the wave, the Abel transformation is used for calculations of the real radial pressure distribution along the line passing through the center of the wave, which is visible at the image, cf. Fig. 12c.

The results of the Abel transformation application to the measured depth-averaged pressure distributions are presented in Fig. 13. The depth-averaged phase distributions are measured in four radial directions with 60° angle interval starting from the bubble center, cf. Fig. 12c. The mean distribution is used for Abel transformation. It is assumed that the reflection from the sapphire windows does not violate the symmetry of the pressure wave. Pressure waves with an amplitude of 100 bar have been detected in the surrounding area of the considered cavitation bubble. Real local pressure values on the wave front can be even higher because the measured distributions are partially smoothed due to the wave motion (≈ 6 μm, cf. Table 1) during the exposure time $t_{\mathrm{exp}} = 5$ ns. The pressure values in the collapsing bubble ($R \lesssim 2$ μm) are not accurate because of the poor quality of the interference fringes. The middle part of $R \leq 20$ μm is removed from the radial pressure distribution, cf. Fig. 13. Rarefaction waves with pressure values compared to the outflow pressure are also detected, cf. Fig. 13.

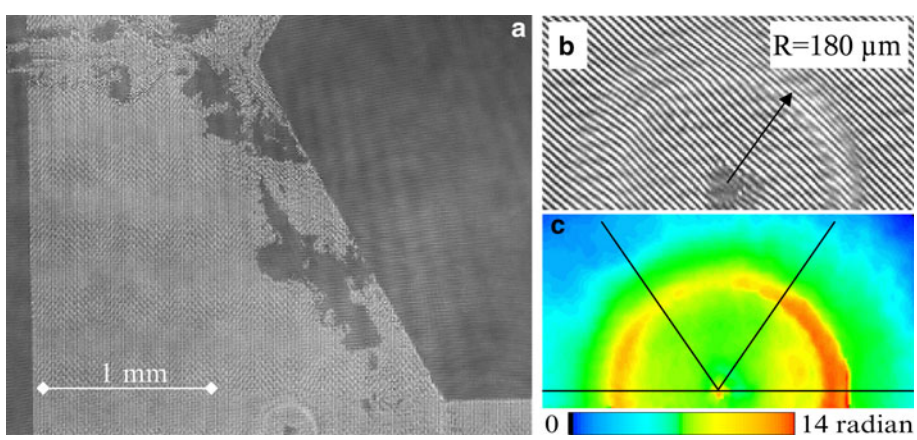

Fig. 12 **a** Original interferogram, **b** magnified part with bubble collapse, **c** evaluated differential phase distribution; $p_{\mathrm{in}} = 336$ bar, $p_{\mathrm{out}} = 36$ bar, and $T_{\mathrm{in}} = 303$ K

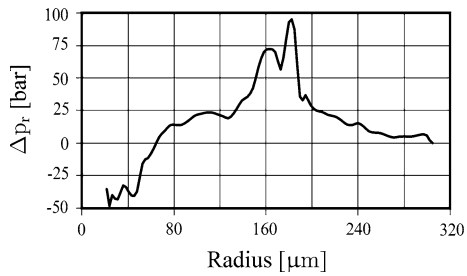

Fig. 13 Radial pressure distribution for the shock wave with the center at the bubble middle

A definite dependence of the wave front local pressure on wave radius is observed. The waves with larger radius always have smaller pressure values. For example, a pressure wave with a radius of $R = 1{,}300$ μm has an amplitude of $\delta p = 30$ bar. Some definite oscillations of spatial pressure distributions during bubble collapses are mentioned for transmission and interferometric images. These results concerning bubble collapse and corresponding shock waves must be considered as preliminary ones, and detailed investigations will be done later. The results are very promising and can be used for further detailed investigations of bubble collapses and cavitation erosion in complex flow geometries.

6 Discussion and conclusion

Flow situations that are typical for nozzle holes in diesel fuel injectors and valves have been studied in an optically accessed planar flow experiment. A pulse interferometry technique has been developed to enable fast pressure field measurements for image exposure times of 5 ns and a spatial resolution of 3 μm. The technique has been applied to a forward-facing step flow and to a target flow situation. Test results are presented in the form of a database for the turbulent pressure fields established in both flow situations. The results provide quantitative data and statistical descriptions for single-shot, mean, standard deviation and single-shot differential density and pressure distributions. The last ones contain information about generated flow turbulences and fluctuations. Quantitative analysis of local flow pressure fluctuations is performed and the inlet turbulence frequency has been extracted. Definite relations between turbulent pressure fluctuations and cavitation onset are found out experimentally. The expansion of shock waves induced by collapsing cavitation bubbles has been visualized by means of the short exposure time and the high spatial resolution. The amplitude of these shock waves has been evaluated with an Abel transformation. The experimental results provide a comprehensive set of quantitative data for the validation of CFD software for compressible three-dimensional multi-phase flow simulation.

References

Belahadji B, Franc JP, Michel JM (1995) Cavitation in the rotational structures of a turbulent wake. J Fluid Mech 287:283–403

Born M, Wolf E (1999) Principles of optics, 7th edn. University Press, Cambridge, p 952

Boehman A, Alam M, Song J, Acharya R, Szybist J, Zello V (2003) Fuel formulation effects on diesel fuel injection, combustion, emissions and emission control, 2003 diesel engine emissions reduction conference, Newport

Budwig R (1994) Refractive index matching methods for liquid flow investigations. Exp Fluids 17:350–355

Brennen CE (1995) Cavitation and bubble dynamics. Oxford University Press, Oxford

Collier RJ, Burckhardt C and Lin LH (1971) Optical holography. Academic Press, New York

Franc J-P (2009) Cavitation erosion: towards a new approach, 7th international symposium on cavitation

Goodman J (1968) Introduction to fourier optics. McGraw-Hill, New York

Hipp M, Reiterer P (2003) User Manual for IDEA 1.7, Technische Universität Graz, http://www.optics.tu-graz.ac.at/idea/Manual_IDEAv17.pdf

Hipp M and Reiterer P (2003) Software for interferometrical data evaluation, Technische Universität Graz, http://www.optics.tu-graz.ac.at/idea

Hipp M, Reiter P, Woisetschläger J, Philipp H, Pretzler G, Fließer W, Neger T (2002) Interferometric fringe evaluation procedures and algorithms subsumed in free software package IDEA, Beitrag im Abstracts-Band im Rahmen wissenschaftlicher Kongresse

Hipp M, Woisetschlaeger J, Reiterer P, Neger T (2004) Digital evaluation of interferograms. Measurement 36:53–66

Iben U, Morozov A (2008) Experimental analysis and simulation of cavitating throttle flow, HEFAT 2008, 6th international conference on heat transfer, fluid mechanics and thermodynamics

Koivula T (2000) On cavitation in fluid power, Proceedings of 1st FPNI-PhD symposium, Hamburg, pp 371–382

Lui S, Li S, Zhang L, Wu Y (2008) A mixture model with modified mass transfer expression for cavitating turbulent flow simulation. Eng Comput 25:290–304

Ostrovsky YI, Butusov MM, Ostrovskaya GV (1980) Interferometry by holography. Springer, Berlin

Vest CM (1979) Holographic interferometry. Wiley, New York

Winklhofer E, Kull E, Kelz E, Morozov A (2001) Comprehensive hydraulic and flow field documentation in model throttle experiments under cavitation conditions, ILASS, Europe, pp 629–634

Woisetschlaeger J, Pretzler G, Jericha H, Mayrhofer N, Pirker HP (1998) Differential interferometry with adjustable spatial carrier fringes for turbine blade cascade flow investigations. Exp Fluids 24:102–109